Research Square

Preprints are preliminary reports that have not undergone peer review.
They should not be considered conclusive, used to inform clinical practice,
or referenced by the media as validated information.

Structures of *in vitro* assembly products of poxvirus scaffolding protein reveal transition from pre-assembly state to fully assembled scaffold

Jaekyung Hyun

jhyu002@skku.edu

Sungkyunkwan University https://orcid.org/0000-0003-2914-537X

Yeontae Jang

Sungkyunkwan University https://orcid.org/0009-0002-4847-1015

Seungmi Kim

Sungkyunkwan University

Seu-Na Lee

Institute for Basic Science

Bumhan Ryu

Institute for Basic Science https://orcid.org/0000-0003-1220-3908

Hyeongseop Jeong

Electron Microscopy Research Center, Korea Basic Science Institute

Eun Sung Kang

Sungkyunkwan University

Jae Hoon Sul

Sungkyunkwan University

Dong-Gyu Jo

Sungkyunkwan University

Yong Ho Kim

Sungkyunkwan University

Article

Keywords:

Posted Date: June 3rd, 2025

DOI: https://doi.org/10.21203/rs.3.rs-6671899/v1

License: This work is licensed under a Creative Commons Attribution 4.0 International License.
Read Full License

Additional Declarations: There is **NO** Competing Interest.

Version of Record: A version of this preprint was published at Nature Communications on September 15th, 2026. See the published version at https://doi.org/10.1038/s41467-026-77815-3.

Abstract

During poxvirus morphogenesis, the external scaffold plays a key role in defining the shape and size of immature virions. However, its structural characterization has been hindered by the pleomorphic nature of authentic virus particles. Here, we present single-particle cryo-electron microscopy and cryo-electron tomography structures of two distinct *in vitro* assemblies of the vaccinia virus scaffold protein D13 that recapitulate oligomeric states previously observed *in situ*. These structures reveal a dramatic transition from rod-like oligomers, representing a pre-assembly state, to a fully formed scaffold, triggered by the docking of N-terminal peptide of the membrane protein A17 into the base cavity of D13. We propose that this interaction destabilizes the pre-assembly conformation and initiates scaffold formation upon viral membrane recruitment, ultimately leading to the immature virion. Our findings provide novel structural insights into the early stages of poxvirus morphogenesis and establish a mechanistic link between conformational changes in D13 and scaffold assembly.

Main

Poxviruses are large, pleomorphic, double-stranded DNA viruses that notably include variola virus, the causative agent of the deadly disease smallpox[1,2]. Despite the eradication of smallpox in the past century, poxviruses remain a significant threat to humanity. The re-emergence of smallpox-like diseases, exemplified by the recent global mpox outbreak and zoonotic transmissions such as orf and cowpox, underscores this risk. Thus, a thorough understanding of the poxvirus replication cycle at the molecular level is crucial for sustained antiviral preparedness.

Vaccinia virus (VACV), the prototypical poxvirus, has served as the principal model for studying poxvirus assembly [3-5]. Morphogenesis begins with the acquisition of the viral membrane derived from the endoplasmic reticulum, coordinated by viral membrane assembly proteins (VMAPs)[6,7]. D13, a trimeric scaffold protein with a double jelly roll fold[8,9], oligomerizes into a hexagonal lattice on the surface of the viral membrane through interactions with the viral transmembrane protein A17. This lattice defines the morphology of crescent-shaped precursors that subsequently expand into spherical immature virions (IVs)[10-12]. In the absence of a viral membrane, D13 forms rod-like aggregates known as inclusion bodies (IBs)[13,14]. Similar IB formation occurs in viral factories when the A17-D13 interaction is disrupted by mutations or the addition of rifampicin[15,16]. Proper scaffolding of IVs is essential for poxvirus proliferation, making it a promising target for anti-poxvirus strategies[17]. However, the molecular mechanisms underlying scaffold assembly remain poorly understood due to the transient and pleomorphic nature of IVs[18,19].

Studies have shown that D13 assembles into diverse architectures, including short rodlets and large spherical shells *in vitro*. These structures closely resemble the rod-like structures observed in IBs and the scaffold on the surface of IV, respectively[9,20]. Here, we report the structures of these assembly products. Our results show that the rodlet structure represents a pre-scaffold state formed from interconnected

dodecamers of D13 trimers. Disruption of this structure by the N-terminal peptide of A17 bound to the base cavity of D13 triggers a conformational rearrangement into the fully assembled scaffold architecture. This discovery provides critical insights into the novel assembly mechanism of immature poxviruses and establishes a foundation for the development of scaffold-targeting inhibitors.

Results

Cryo-electron tomography of two *in vitro* D13 assembly products. As described in our previous studies[9,20], recombinant D13 trimer was purified in a high-salt buffer and subjected to dialysis to remove excess salt. This process yielded two distinct D13 assembly products. The D13 trimer with an N-terminal His_6-tag assembled into large spherical particles, whereas tag-free D13 trimers formed heavily crowded rod-like structures. These structures recapitulate the native oligomeric states of D13 observed *in situ*, namely the IV scaffold and the rod-like structure found in IBs. The discrepancy in these assembly products was suggested to be due to the His_6-tag that influences the structural stability of the N-terminal α-helix within its binding pocket[20]. To investigate the detailed structures of these *in vitro* D13 assembly products, we performed cryo-electron tomography (cryo-ET).

Tomographic reconstruction of the spherical particles shows strong morphological resemblance to the VACV IV scaffold[19,20]. However, unlike IVs, which display a unilamellar scaffold covering the underlying viral membrane, majority of the *in vitro*-assembled particles were partially composed of two or more layers of scaffold lattice (Fig. 1a). Despite this discrepancy, the average diameter of the spherical particles was approximately 340 nm, which agrees with the reported dimensions of VACV IVs (Extended Data Fig. 1a)[11,19]. Accordingly, we term these assembly products “scaffold-like particles (SLPs)”. Given that SLPs are formed from a semi-regular lattice, we conducted subtomogram averaging (STA) of hexagonal lattice patches, which yielded a 14 Å resolution map (Extended Data Fig. 1b, c). The lattice consists of six copies of D13 trimers organized around an approximate six-fold symmetry axis at the center of the hexagonal ring (Fig. 1b). The reconstruction exhibits mild curvature that tapers toward the membrane-binding base of the D13 trimers. Plotting the STA map onto the tomogram shows that the particles are not perfectly continuous and closed. Instead, small lattice patches are loosely connected, often via vertically overlapping layers (Fig. 1c). These results support the hypothesis that D13 self-assembly serves as the primary driver of the spherical shape[9,20], although the viral membrane must play a critical role in the morphogenesis of the authentic IVs.

Tomographic reconstruction of the rod-like particles showed that they are composed of linear extensions of small hexagonal patches (Fig. 1d). Repeating units within the rodlets prompted us to perform STA, which yielded a map at 13 Å resolution (Extended Data Fig. 2a). Superposition of the D13 trimer structure (PDB 7VDF) into the map revealed that the repeating unit comprises two apposed hexagonal rings (Fig. 1e, Extended Data Fig. 2b), each containing six copies of D13 trimers connected via lateral intertrimeric contacts at the head and base domains. These rings are vertically connected, separated by an approximately 12 Å gap between their membrane-binding surfaces and rotated by 19.3°,

preventing axial alignment. Additional D13 trimers are tethered to the periphery of the rings. While the trimers within the ring lie nearly horizontally, peripheral trimers are attached at a 21.5° torsion angle (Extended Data Fig. 2c). STA map projection onto the tomogram revealed laterally interconnected dodecamers with torsion, forming a chain-like ultrastructure, which we term "twister" (Fig. 1f). This morphology closely resembles the rod-like D13 aggregates in IBs, previously observed in cryo-ET of VACV-infected cells, where D13 trimers are membrane-free[14]. Both twister and rod-like structures in IBs exhibit linear arrangements of hexagonal patches and may represent a pre-assembly state of the D13 scaffold, potentially serving as an intermediate preceding the formation of the IV scaffold.

Cryo-EM structure of scaffold-like particle. Single-particle analysis (SPA) of lattice patches of the SLP enabled a reconstruction of a cryo-EM map at 2.9 Å resolution, allowing detailed examination of intertrimeric interactions and overall D13 trimer organization (Fig. 2, Supplementary Fig. 1). Subtle variations between alternating trimers imparted threefold symmetry to the center of the hexagonal ring. We found average centroid distances of 79.3 Å and 75.2 Å between the head domains and base domains of interacting trimers, respectively, resulting in a torsion angle of 2.6° (Extended Data Fig. 3), which is significantly milder than the torsion angles ranging from 7.6° to 13.5° observed in previously reported tubular assembly products[20].

The cryo-EM structure revealed alternating mode 1 and mode 2 intertrimer interfaces (Fig. 2a), primarily mediated by electrostatic interactions between loops of the head domain and the N-terminal jelly roll (J_N) domain (Fig. 2b, Extended Data Fig. 4). Due to the asymmetric nature of the interfaces, each mode comprises five distinct contact sites, two at the head-to-head region, two at the base-to-base region and one between the C-terminal jelly roll (J_C) domains. Each contact site is labeled with Roman numerals in Fig. 2b. In the mode 1 interface**,** R353 from one trimer interacts electrostatically with N145 and E77 (panel i), while at a second contact site, R353 and R404 from the adjacent trimer form a hydrogen bond network with D325 and N145/P144 (panel ii). At the base domain, D501 and R498 form salt bridges with R59 and D60, respectively, and R498 additionally engages in a cation- p interaction with Y62 (panel iii). Another base-to-base contact involves a hydrogen bond between Y62 and R498 (panel iv). The fifth site involves a hydrogen bond between N456 and E444 located in the J_C b-strands (panel v).

In the mode 2 interface**,** T352, R404 and N355 in one trimer form hydrogen bonds with P145, N144 and Q324 in the neighboring trimer (panel vi). Although R353, K354 and D325 are clustered nearby, specific interactions could not be modeled. At the second head-to-head site, R353 and N355 form electrostatic interactions with N145 and D325, respectively (panel vii). At the base, D60 and Y62 form hydrogen bonds with N449, D450 and D498 (panel viii) while S497 and R498 interact with R59, D60 and Y62 (panel ix). The fifth contact in mode 2 involves J_C b-strand interactions between adjacent trimers (panel x). Both modes of interface share interactions that involve residues including Y62, D325, R353 and R498. These residues have been shown to be critical for D13 self-assembly via site-directed mutagenesis[20] and are conserved among scaffold proteins of poxviruses, highlighting their universal importance across the poxvirus genera[21].

The SLP map shows that a density that corresponds to the N-terminal helix of one trimer remains positioned within its hydrophobic pocket while the corresponding helix density on the opposing trimer is absent (Fig. 2c, d). The weak density precludes accurate structure modeling to address structural changes in comparison to the intact helix of the singular trimer[20]. **Regardless, the result indicates that removal of only one copy of the N-terminal helix is sufficient to promote intertrimeric connection.** We also observed an unassigned density in the central cavity at the base of the D13 trimer, surrounded by phenylalanine residues that form the F-ring that is critical for the binding of rifampicin and the N-terminal tail of A17 (Fig. 2 c, e)[22]. Given the absence of rifampicin or A17 in our samples, we speculate that the density corresponds to the N-terminal a-helix that was translocated from its original binding pocket. To test if this translocation affects the SLP assembly, we produced a chimeric protein in which enhanced green fluorescent protein (eGFP) is linked to the N-terminus of D13, thereby preventing the N-terminal helix from accessing the base cavity. Under the same assembly condition, eGFP-D13 consistently formed SLP, the structure of which remains indistinguishable from the SLP produced from His_6-tagged D13, except that the base cavity is unoccupied (Extended Data Fig. 5, Supplementary Fig. 2). This result indicates that dislocation of the N-terminal helix from its original binding pocket is indeed essential for scaffold formation, but its translocation into the base cavity is not a prerequisite.

Cryo-EM structure of the twister assembly. Images of the dodecameric rings of D13 trimers that form the twister were used to reconstruct a single-particle cryo-EM map at 3.9 Å resolution (Fig. 3a, Supplementary Fig. 3a, b). We found that all N-terminal α-helices involved in intertrimeric interactions within the hexagonal ring are absent from their original binding pockets, while those at the periphery remain intact (Fig. 3b). Intriguingly, we found additional map density at the rifampicin-binding base cavity of D13 trimers[22] (Fig. 3c). Although the local density was insufficient for atomic modeling, its weak yet continuous connection to the trimer above suggests that it represents the N-terminal α-helix from the vertically apposed trimer. To assess the structural feasibility of this insertion, we performed a molecular dynamics (MD) simulation using a model in which the N-terminal α-helix was manually positioned within the base cavity of D13 (Extended Data Fig. 6a). Throughout the simulation, the helix remained stably accommodated within the rifampicin-binding cavity without dissociation under approximately 6Å, supporting our interpretation of the cryo-EM map density (Extended Data Fig. 6b). The density at the cavity is connected to F486, which appears to serve as a key interaction site for helix insertion (Fig. 3d). To test whether F486 is functionally essential for twister formation, we analyzed the assembly morphology of a mutant protein in which phenylalanine residue was substituted with alanine (F486A). The mutant failed to form twister-like structures and instead produced laterally extended net-like aggregates, likely due to the loss of vertical interactions (Extended Data Fig. 6c).

Intertrimeric interactions within the twister assembly. To improve the map quality, we performed focused refinement to resolve the intertrimeric interfaces within the twister. This approach yielded structures of three interacting trimer pairs at resolutions ranging from 2.9 to 3.2 Å (Supplementary Fig. 3c, d). We identified three modes of intertrimer interfaces (mode I, II and III) that are distinct from the interfaces in the SLP (mode 1 and 2). Mode I and mode II are involved in the hexameric ring assembly,

and mode III is responsible for the tethering of a peripheral trimer (Fig. 3e, Extended Data Fig. 7). The mode I interface closely resembles the VACV D13 doublet structure (PDB: 7VFG) (Extended Data Fig. 8a), while mode II resembles the asymmetric interface observed in the tubular assembly (PDB: 7VFH) (Extended Data Fig. 8b)[20]. The mode III arrangement loosely follows the trimer packing seen in the crystal structure (PDB: 6BEI) (Extended Data Fig. 8c)[22]. Each contact site is labeled with Roman numerals in Fig. 3f-h. The two trimers in the mode I interface are arranged with two-fold symmetry and a torsion angle of 8.3° (Extended Data Fig. 8d). Head loops of adjacent trimers interact through a hydrogen bond between N355 and the carboxyl group of Q324 (panel i), while R353 and N355 are positioned near D325, suggesting potential salt bridge and hydrogen bond interactions. Additionally, the carboxyl group of T352 forms a hydrogen bond with N145 of the neighboring trimer. In the intermediate region, where the β-sheet trunks of the J_C domains contact, a cluster of charged and polar residues (R442, E444, R446, and S454) forms a network of electrostatic interactions (panel ii). At the base-to-base interface, R498 engages in a cation-p interaction with Y62, while a salt bridge between D501 and R59 further stabilizes the contact (panel iii).

In the mode II interface, adjacent trimers are related by 14.1° torsion and a vertical offset, resulting in an asymmetric alignment (Extended Data Fig. 8e). The head loop of each trimer interacts with the proximal J_N domains via distinct contacts. At one site, S356 forms a hydrogen bond with N145 (panel i in Fig. 3g), while at the other, R353 and N355 engage in a salt bridge and hydrogen bond with D205 and P144, respectively (panel ii in Fig. 3f). Similarly, the base domains form asymmetric interactions. R498 and D501 form salt bridges with D60 and R59, respectively (panel iii in Fig. 3f). At the other site, R498 and R446 form a hydrogen bond and a salt bridge with the hydroxyl group of Y62 and D60, respectively (panel iv in Fig. 3f). Compared to mode I, the mode II interface involves fewer residues and lacks interaction between the β-sheet trunks of the J_C domains. As a result, the intertrimeric binding surface area is smaller in mode II (964 $Å^2$) than in mode I (1306 $Å^2$).

In the mode III interface, a peripheral trimer attaches to the edge of the hexameric ring at either a lower or higher position, producing a pronounced warp of 23.4° and deviating markedly from planarity (Extended Data Fig. 8f). This interface spans 1396 $Å^2$, the largest among the three modes. For clarity, residues from the upper trimer are denoted with a prime symbol (’). The head loop of the lower trimer inserts into a groove between the jelly roll domains of the upper trimer, forming hydrogen bonds involving S356, F357, I356, S441’, T511’, and N515 (panel i in Fig. 3g). Additional contacts include a salt bridge between E74’ and R404, and a hydrogen bond between Q241’ and N145 (panel ii and iii in Fig. 3g). D513 is located adjacent to R442’, suggesting a potential salt bridge (panel iv in Fig. 3g). Notably, substituting D513 with glycine induces aberrant planar lattice formation, indicating a pivotal role in this distinctive skewed interaction[13]. The N-terminal α-helix remains embedded in its original pocket. Residues N3’ and M1’ from the helix form hydrogen bonds with N441 and R442 of the neighboring trimer, respectively (panel v in Fig. 3f). Additional electrostatic and hydrophilic interactions (R442–D60’, R446–D175’ and R498’–S40/P210) further stabilize the intertrimeric contact (panel vi and vii in Fig. 3f). We

propose that retention of the N-terminal helix facilitates the skewed lateral interaction, reinforcing weak vertical association between hexagonal D13 rings.

Molecular mechanism of transition from twister to scaffold. We investigated the mechanism by which the twister (i.e., pre-scaffold) transitions into the scaffold during IV assembly. Since the N-terminus of A17 interacts with the base cavity of D13 to facilitate localized scaffold assembly on the viral membrane[16,22], we hypothesized that this interaction drives the morphological transition by replacing the N-terminal helix of D13 in the twister bound to the same base cavity. To test this, we synthesized a polypeptide comprising the first eight N-terminal residues of A17 ($A17_{1\text{-}8}$), which are most critical for D13 binding[22] and introduced it to the pre-assembled twister complex. Remarkably, this led to a structural transformation into SLPs, strongly supporting the role of A17 in reorganizing the D13 arrangement beyond its previously reported function in membrane recruitment.

We then performed single-particle cryo-EM on the resulting trimers (i.e., supernatant of the assembly mix) and SLPs (i.e., pellet), yielding reconstructions at 2.5 Å and 3.7 Å resolution, respectively (Fig. 4a, d, Supplementary Fig. 4, 5). In $A17_{1\text{-}8}$-bound D13 trimer, a clear additional density was observed at the rifampicin-binding base cavity, while the overall D13 structure remained unchanged to the peptide-free structure (Extended Data Fig. 9a). However, the density appeared highly symmetrized, likely due to a local minima problem caused by its position along the symmetry axis, precluding accurate atomic model building. Nevertheless, we found the density is proximal to the residues known to be critical for A17 binding[22,23] (Fig. 4b). Interestingly, an additional density was also observed in a narrow groove within the head domain (Extended Data Fig. 9b). The residues proximal to this density are primarily polar and hydrophobic, suggesting potential hydrophobic interaction involving tyrosine residues at the N- and C-termini of $A17_{1\text{-}8}$ (Fig. 4c, Extended Data Fig. 9c). However, the discontinuity of the density prevents reliable atomic modeling, and the functional significance of this secondary binding site remains unclear.

The $A17_{1\text{-}8}$-bound SLP structure closely resembles SLPs produced by His_6-tagged D13 (RMSD 1.051) (Extended Data Fig. 10a). Consistent with the singular D13 trimer, densities were also observed at the base cavities of trimers in the hexagonal lattice (Fig. 4e, Extended Data Fig. 10b). Several additional densities were detected, but at positions from those in the singular trimer. One of these densities was found within the hydrophobic pocket that typically accommodates the N-terminal α-helix (Fig. 4g, Extended Data Fig. 10c). While this density may correspond to a residual N-terminal helix, it may also represent a segment of the $A17_{1\text{-}8}$, peptide that occupies the pocket and facilitates helix removal, thereby promoting the twister-to-SLP transition. The other densities are located at the head-to-head intertrimeric interfaces (Fig. 4f, Extended Data Fig. 10d), suggesting that A17 may modulate intertrimeric rearrangement.

Discussion

Recent advances in cryo-EM and cryo-ET have enabled unprecedented visualization of mature poxvirus structure[24-27]. However, high-resolution structure determination of IV remained limited. In this study, we report the structures of two self-assembly products of recombinant VACV D13 that recapitulate *in situ* architectures. The twister assembly represents a membrane-free D13 structure within the viral factory, whereas the SLP corresponds to the fully assembled scaffold on the viral membrane. Furthermore, we demonstrated a structural transition between these states driven by the N-terminal tail of A17 ($A17_{1-8}$), with translocation of the D13 N-terminal α-helix playing a key role in this process. Based on these findings, we propose a mechanism for the scaffold formation (Fig. 5). Under physiological conditions, D13 likely exists as aggregated twisters before membrane recruitment, ensuring its high local concentration within the viral factory. Lateral intertrimeric interactions and additional base-to-base vertical interactions via the N-terminal α-helix promote the assembly of oligomer composed of twelve copies of D13 trimer. The intact N-terminal α-helices at the periphery of the dodecamer induce twisted tethering of additional trimers, forming rodlets. This conformation prevents single-layered scaffold lattice expansion, thus inhibiting premature scaffold shell assembly in the absence of the viral membrane. Upon membrane recruitment, the N-terminal tail of A17 displaces the N-terminal α-helix of D13, disruption of the vertical interactions of twister. A17 may further facilitate this transition by engaging in lateral intertrimeric interactions, as suggested by additional densities observed in $A17_{1-8}$-bound SLP.

Our results suggest that D13 and A17 are sufficient to establish the spherical shape of the IV. However, additional proteins must be involved in proper IV formation *in situ* through membrane-mediated mechanisms linked to D13–A17 interaction. Notably, A17 is known to interact with a number of late viral proteins[28-30], and can induce membrane deformation characterized by high curvature and tight lipid packing[31]. To enable D13 attachment to the convoluted viral membrane precursors, additional modulators may coordinate membrane curvature. VMAPs, beyond their role in membrane scission, may fulfill this function. Moreover, recent studies suggest that the D13 lattice may also impose spatial constraints on the MV, suggesting a potential link to core proteins A10 and A4 [19,32]. Involvement of H7 has also been proposed to be essential for hexamerization of D13 trimers[33], indicating an additional mechanism of scaffold assembly.

Brincidofovir and tecovirimat are currently the only available antivirals for smallpox that target viral DNA polymerase and the wrapping of mature virion, respectively. However, their efficacy against other poxvirus infections remains unproven and resistant mutations to tecovirimat are increasingly reported[34,35]. In this context, the scaffold protein represents an attractive target for novel antiviral development, as demonstrated by rifampicin's ability to arrest virion assembly. Our study provides a foundation for the design of next-generation antiviral agents analogous to capsid-targeting drugs such as lanacapavir for HIV-1. Furthermore, the conservation of intertrimeric interfaces across poxvirus genera suggests the potential for developing broad-spectrum antiviral agents.

Methods

Cloning The gene encoding D13 of Western Reserve strain Vaccinia virus was inserted in the pPROEX-Hta vector using SfoI and HindIII restriction enzymes as described previously[9]. To produce $D13F_{486A}$ mutant protein, we introduced alanine substitution mutations at F486 residue using Q5 site-directed mutagenesis kit (NEB). For the chimeric EGFP-D13 protein production, EGFP and D13 sequences were PCR-amplified from the plasmid pSpCas9(BB)-2A-GFP (PX458) (Addgene plasmid #48138) and D13 in pPROEX-Hta, respectively. Then, the two products were extended by overlap extension PCR. The resulting overlapped insert was cloned into the original D13 vector (pPROEX-Hta) after digestion with EcoRI and HindIII enzymes. Primers used for the construct modification are listed in supplementary table 1.

Protein expression and purification. The genes encoding both the wild-type and mutant D13 in the pPROEX-Hta vector were expressed in BL21 (DE3) cells, whereas EGFP-D13 was expressed in Rosetta (DE3) cells. Gene products were purified using immobilized metal affinity chromatography (IMAC) using a gravity column filled with Nickel agarose (QIAGEN). Except for His_6-tagged D13, Tobacco etch virus (TEV) protease digestion was conducted to remove N-terminal His_6 tag. The protein was further purified by size exclusion chromatography using a protein storage buffer containing 50 mM Tris-HCl (pH 8.0), 500 mM NaCl, 25 mM L-arginine, 25 mM L-glutamic acid and 2 mM β-mercaptoethanol.

Materials for peptide synthesis. H-Rink amid ChemMatrix® resin (0.1 mmol, 0.45 mmol/g) was obtained from PCAS BioMatrix Inc. Solvents including dimethylformamide (DMF), methanol (MeOH), acetonitrile (ACN), and ethanol (EtOH) were sourced from Daejung. Amino acids and O-(1H-6-chlorobenzotriazole-1-yl)-1,1,3,3-tetramethyluronium hexafluorophosphate (HCTU) were acquired from AAPPTec. Additionally, N,N'-diisopropylcarbodiimide (DIC, ≥98.0%), piperidine (≥99.0%), trifluoroacetic acid (TFA, 99%), and triisopropylsilane (TIS, 98%) were purchased from Sigma Aldrich. Ultrapure deionized water was produced using a Millipore Milli-Q purification system.

Peptide Synthesis. Peptide sequence was synthesized via Fmoc-based solid-phase peptide synthesis (SPPS) using H-Rink amid ChemMatrix® resin (0.45 mmol/g). The synthesis was performed with a Syro I fully automated parallel peptide synthesizer (Biotage). Prior to synthesis, the resin was swollen in DMF for 20 minutes. The deprotection process involved two sequential steps: an initial treatment with 20% piperidine in DMF for 5 minutes, followed by exposure to 40% piperidine for 10 minutes. Coupling reactions were performed with HCTU (5 equivalents), N-methylmorpholine (NMM, 10 equivalents), and the respective amino acid (5 equivalents) in DMF, with each reaction lasting 8 minutes and repeated twice. Unreacted reagents were eliminated through multiple washes with DCM and DMF. Following peptide assembly, PNA monomers were sequentially incorporated at the peptide's N-terminal while still linked to the resin, following a standard PNA synthesis protocol. The deprotection steps for PNA synthesis consisted of two treatments: 40% piperidine for 15 minutes, followed by 20% piperidine for an additional 15 minutes. PNA monomer coupling was carried out using HCTU (5 equivalents), NMM (10 equivalents), and amino acid (5 equivalents) in DMF for 90 minutes, ensuring efficient attachment. Any residual reagents were thoroughly removed by repeated washes with DCM and DMF. To cleave the final product from the resin, a cleavage cocktail composed of TFA:TIS:deionized water (95:2.5:2.5, v/v) was applied for 2.5 hours. The resin was subsequently removed by filtration, and the filtrate was concentrated

under a nitrogen stream. The crude product was precipitated with ice-cold diethyl ether and dried under vacuum. Purification was achieved via reverse-phase high-performance liquid chromatography (RP-HPLC) using a Waters Quaternary Gradient Module 2545 system with a C4 reverse-phase column. A linear gradient of 0.5%/ml was applied, starting from a solvent composition of 60% solvent A (distilled water/TFA, 99.9/0.1, v/v) and 40% solvent B (isopropanol/ACN/distilled water/TFA, 60/30/10/0.1, v/v). The molecular weight of the synthesized M2TM-PNA conjugate was verified through matrix-assisted laser desorption/ionization-time of flight (MALDI-TOF) mass spectrometry. A summary of the synthesized peptide sequence and its theoretical molecular weights is provided in *supplementary table 2*.

D13 self-assembly. A 100 µL aliquot of purified protein at approximately 5 mg/mL was dialyzed in a buffer containing 10 mM Tris-HCl (pH 8.0), 150 mM NaCl, and 2 mM β-mercaptoethanol at 4°C for at least 12 h. The resulting assembly mix was centrifuged at 18,472 xg for 30 min at 4°C. The pellet was collected and resuspended with 20 µL of the storage buffer for the Cryo-EM and Cryo-ET analysis. The supernatant was used for the structural analysis of singular, unassembled trimers. For the preparation of $A17_{1\text{-}8}$ peptide-bound D13 assembly products, pre-assembled twister was resuspended in the storage buffer supplemented with 1.8 mM $A17_{1\text{-}8}$ peptide, followed by incubated at 4°C for 20 h.

Cryo-electron microscopy. For tomographic analysis of SLP, His_6-tagged D13 assembly product **was** mixed with 5 nm gold fiducials (AURION) at a 4:1 (v:v) ratio. 3µL of the mix was applied onto Quantifoil R2/2 Cu 300 mesh holey EM grid (Quantifoil Micro Tools GmbH) without glow discharge. The sample was vitrified using a Vitrobot Mark IV (Thermo Fisher Scientific, TFS) at 4 °C and >90% humidity. Tilt series images were acquired using a Krios G4 TEM (TFS) operating at 300 kV, at 42,000× nominal magnification (2.12 Å/pixel), using a dose-symmetric tilt scheme from −54° to +54° with 3° increments. The applied defocus ranged from −1.5 to −2.5 µm. Images were recorded on a K3 BioQuantum direct electron detector (Gatan) in electron counting mode, using a zero-loss energy filter (20 eV slit width). The total dose was approximately 120 $e^-/Å^2$ per tomogram, with 5 movie frames collected per tilt image. **A total of 33 tilt series were acquired using Tomography5 software (TFS).**

For tomographic analysis of twister, the sample was mixed with 10 nm gold fiducial markers (AURION) at a 1:1 (v:v) ratio. 3µL of the sample was applied to a Quantifoil R1.2/1.3 Cu 300 mesh EM grid (Quantifoil) and vitrified using Vitrobot Mark IV (TFS) at 4 °C and >90% relative humidity. Tilt series were acquired on a Krios G4 TEM (TFS), operated at 300kV acceleration voltage, equipped with a Falcon 4i direct electron detector (TFS), at a magnification of 59,000× (1.36 Å/pixel). The applied defocus ranged from −2.5 to −3.5 µm. Tilt images were acquired using a dose-symmetric scheme with a tilt range from −60° to +60° with tilt 3° increments. A cumulative electron dose of approximately 120 $e^-/Å^2$ was applied per tilt series. **A total of 11 tilt series were acquired using Tomography5 software (TFS).**

For SPA of SLP, 3µL of the sample was applied to a Quantifoil R1.2/1.3 Cu 300 mesh grid **without** glow discharge and vitrified using the abovementioned conditions used for tomography analyses. Movie data were collected on a 300 kV Krios G4 TEM (TFS) equipped with a K3 BioContinuum direct electron detector (Gatan). Images were recorded at a nominal magnification of 42,000× in super-resolution mode,

corresponding to a physical pixel size of 1.045 Å. The defocus range was set from −1.5 to −2.5 µm. A Gatan GIF energy filter (20 eV slit width) was used for zero-loss imaging. Movies were recorded using EPU software (TFS) in **LZW-compressed TIFF format,** with 50 frames per movie, with a total dose of 38.6 e^-/Å per a movie. **A total of 512 movies were acquired.**

For SPA of eGFP-D13 SLP, 3µL of the sample was applied to a freshly glow discharged Quantifoil R1.2/1.3 Cu 300 mesh EM grid (Quantifoil) and vitrified using the same conditions as for sample grid preparation used for the SPA of SLP. Data were collected on a 300 kV Krios G4 TEM (TFS) equipped with a K3 BioContinuum direct electron detector (Gatan). Images were recorded at a nominal magnification of 42,000× in super-resolution mode, corresponding to a physical pixel size of 1.045 Å. The defocus range was set from −1.6 to −2.6 µm. A Gatan GIF energy filter (20 eV slit width) was used for zero-loss imaging. Movies were recorded using EPU software (TFS) in **LZW-compressed TIFF format,** with 50 frames per movie, a total dose of 50 e^-/Å². **A total of 1,094 movies were acquired.**

For SPA of the twister assembly, the sample was vitrified following the same protocol as used for the preparation cryo-ET samples. Cryo-EM data for the SPA of twister were collected using a Krios G4 TEM (TFS) equipped with a Falcon 4i (TFS) operated at 300 kV acceleration voltage. Images were recorded at a nominal magnification of 59,000×, corresponding to a pixel size of 1.33 Å, with the defocus range was set between -1.4 and -2.2 µm. The total electron dose of 50 e^-/Å² was applied for imaging. Data acquisition was performed using the EPU automated acquisition software (TFS). A total of 9,411 movies were recorded in EER format, from which the raw movie frames were fractionated into 50 MRC format fractions per a movie.

$A17_{1\text{-}8}$-bound D13 trimers and SLP were separated by centrifugation 18,472xg, for 30min after peptide incubation. The supernatant containing the singular trimers was applied onto a Quantifoil R1.2/1.3 Cu 300 mesh EM grid (Quantifoil) with additional graphene oxide-supported film (Sigma Aldrich). A total of 13,356 movies were collected using a Glacios TEM (TFS), operated at 200 kV, with a Falcon 4i direct electron detector (TFS), at a nominal magnification of 92,000×, corresponding to a pixel size of 1.067 Å. The total electron dose of 51.49 e^-/Å² was fractionated into 50 frames in LZW-compressed TIFF format. The applied defocus range was set between -1.2 and -2.2 µm. The pellet containing the $A17_{1\text{-}8}$-bound SLP was applied to a freshly glow discharged Quantifoil R1.2/1.3 Cu 300 mesh grid (Quantifoil). A total of 2,799 movies were collected using 300 kV Titan Krios TEM (TFS) equipped with a K3 BioContinuum direct electron detector (Gatan). Images were recorded at a nominal magnification of 42,000× in super-resolution mode, corresponding to a physical pixel size of 1.045 Å. The defocus range was set from -1.5 to -2.5 **µm**. A Gatan GIF energy filter (20 eV slit width) was used in zero-loss mode. Movies were recorded using EPU software in **LZW-compressed TIFF format**, with 50 frames per movie, a total dose of 50 e^-/Å².

Cryo-ET image processing. For tomographic reconstruction and subtomogram averaging of SLP, cryo-ET data was processed using RELION-5.0[36]. Raw movie frames and associated metadata were imported into RELION-5.0 tomography project. A total of 33 raw movie frame sets were processed, and metadata describing the tilt series were standardized in star format for downstream analysis. Motion correction

was performed using RELION's built-in tools or UCSF MotionCor2[37]. Contrast transfer function (CTF) was estimated using RELION's wrapper for CTFFIND4.1.14[38]. Tilt series alignment was conducted using IMOD[39] wrappers in RELION, utilizing fiducial-based alignment. Corrections for stage tilt axis orientation were applied to optimize alignment accuracy. Tomograms were reconstructed using real-space weighted back-projection with CTF pre-multiplication. Initially, the pixel size was binned to 10 Å to improve computational efficiency. Tomogram denoising was performed using cryo-CARE[40] to improve contrast and enhance structural features for downstream analysis. Particle picking was performed using Napari-based tools with the picking mode set to "sphere" and a particle spacing of 150 Å, resulting in 81,939 annotated particles. Particles were extracted with a final box size of 128 pixels, obtained by 2x Fourier cropping from 256-pixel boxes and subjected to a second round of 3D refinement. Duplicate particles within a 150 Å spacing were removed, reducing the dataset to 71,124 particles. A subsequent 3D classification step excluded poorly aligned sub-volumes, resulting in 63,008 assorted particles for further analysis. Another round of duplicate removal with 250 Å spacing, followed by 3D classification to remove poorly aligned particles. Final refinement was performed using 39,393 particles, yielding a map at 14 Å resolution (FSC = 0.143). To visualize the positions and orientations of particles within the tomograms, we used ArtiaX, a ChimeraX plugin[41].

For tomographic reconstruction and subtomogram averaging of the twister, five frames per each tilt image were motion-corrected and summed using MotionCor2. Motion-corrected images were re-stacked according to the original tilt order using *newstack* function in IMOD. Newly generated tilt series images were imported to the etomo program in the IMOD package and aligned using both patch- and fiducial-based methods. A SIRT-filtered back projection approach was employed to generate tomograms with a down sampling factor of 2. For subtomogram averaging, the motion-corrected tilt series images were imported to EMAN2[42]. After coarse alignment, patch tracking and fiducial tracking, the aligned tilt series were reconstructed into 4x binned tomograms. After CTF estimation, the published D13 sextet map (EMD-31954) was used as a 3D template for reference-based particle annotation. A total of 2,500 initial particles were extracted into168-pixel cubes and refined to yield a 15.8 resolution map. Using this map as new reference, 3,499 particles were picked and extracted, leading to a 13.8 Å resolution reconstruction. Ortho-projection classification was applied, and 1,620 selected particles were further refined. To visualize the positions and orientations of particles within the tomograms, the built-in *Map Particles to Tomograms* function was utilized. The half-maps and mask in HDF format were converted to MRC format, and the final resolution was estimated to be 13 Å (FSC=0.143) using the Relion5 postprocess command-line tool.

Single-particle Cryo-EM image processing. Single-particle cryo-EM data of SLPs were processed using CryoSPARC v4.5.3[43]. A total of 512 super-resolution movies were motion-corrected and the resulting images were subjected to CTF estimation. Particles were picked using the blob picker with a diameter range between 80 and 250 Å, yielding 1,209,388 particles. To enable accurate centering of hexagonal lattice patches particles were initially extracted with a large box size of 800 pixels, and Fourier-cropped to 400-pixel during extraction. After three rounds of 2D classification, 860,633 particles were selected

and subjected to an ab-initio reconstruction and heterogeneous refinement without symmetry imposition. The assorted 808,264 particles were used for non-uniform refinement with C3 symmetry. The resulting particles were re-extracted, and duplicates within 20 Å were removed, leaving 739,115 particles. After two rounds of global and local CTF refinement followed by non-uniform refinement, the map resolution improved to 3.01 Å. To remove residual junk particles, a low-pass filtered disc-shaped map was generated using UCSF Chimera and used for heterogeneous refinement. The 722,411 particles that belong in the 3D class with detailed structural features were refined with local refinement and recentering using a binary mask, resulting in a final map at 2.88 Å resolution (FSC = 0.143).

For eGFP-D13 SLP, 1,094 raw movies were imported to CryoSPARC v4.5.3 and subjected to patch motion correction and patch CTF estimation using default parameters. From 709 curated micrographs, particles were picked using the blob picker with a diameter range between 80 and 250 Å. 1,671,619 particles were initially extracted and subjected to 2D classification, from which 320,527 particles were selected for *ab initio* reconstruction and non-uniform refinement with C1 symmetry. The particles that belong in the major class were further refined using non-uniform refinement with C3 symmetry. Particles were re-extracted without down-sampling, into 400-pixel boxes, and subjected to global and local CTF refinement in between three additional rounds of non-uniform refinement with C3 symmetry imposition. Then, duplicate particles were removed using a 20 Å distance cutoff, and reference-based motion correction was performed. Final round of CTF refinement and non-uniform / local refinement yielded a map at 3.70 Å resolution (FSC = 0.143).

For the SPA of the twister, the original EER movie files of twister were converted to TIFF format using the built-in *relion_convert_to_tiff* command in Relion4 and the subsequent process employed cryoSPARC v4.5.3 software. The movies were pre-processed by patch motion correction and patch CTF estimation, and a total of 9,294 movies were selected for further processing. Template picking was performed using 2D templates obtained from class averages of a subset data, resulting in the extraction of 1,500,729 particles with down sampling factor of 2. After two rounds of 2D classification, 359,284 particles were selected and extracted into 360-pixel boxes. Following two rounds of heterogeneous refinement, 105,518 selected particles that belong in the class that exhibit most pronounced structural detail were subjected to homogeneous refinement, and global and local CTF refinements. Subsequently, 104,933 reference-based motion-corrected particles were used to obtain a 3.9 Å consensus map. Further processing involved local refinement, CTF refinement, and signal subtraction using progressively smaller masks (sextet and doublet). During this step, only mode I was refined with C2 symmetry imposition due to clear symmetric arrangement of the trimers. As a result, we generated the final maps with resolutions of 2.9 Å, 3.2 Å, and 3.1 Å for Mode I, II, and III, respectively.

For $A17_{1\text{-}8}$-bound D13 trimer, raw movies were imported to CryoSPARC v4.5.3 and subjected to patch motion correction and patch CTF estimation. We used published wildtype D13 trimer map (EMD-31949) as an initial template for particle search, and generated 2D templates from subset of 500 micrographs. Using the new template, 4,387,513 particles were extracted into 256-pixel boxes from 12,336 micrographs. After two rounds of 2D classification, 2,419,699 particles were selected for further

processing. We sorted particles through heterogeneous refinement to remove trimers that too close to another. The assorted 2,072,322 particles were subjected to CTF refinement and homogeneous refinement, resulting in 2.63 Å resolution map. After removal of duplicate particles and reference-based motion correction, final reconstruction was generated from 2,044,397 particles without symmetry imposition, at 2.48 Å resolution.

For $A17_{1-8}$-bound D13 SLP, raw movies were imported into CryoSPARC v4.5.3 and processed using patch motion correction and patch CTF estimation with default parameters. From 2,787 curated micrographs, a subset of 300 was used to generate an *ab initio* model, which was also utilized to create 2D templates for particle picking with a 250 Å diameter setting. This yielded a total of 2,182,420 particles from the full dataset. After two rounds of 2D classification, 1,512,824 particles were selected and subjected to 3D classification with C1 symmetry. Among the resulting classes, 690,859 particles representing the major class were selected for non-uniform refinement. Then, the particles were then re-extracted without down-sampling, into 400-pixel boxes, followed by global and local CTF refinement and three additional rounds of non-uniform refinement with C3 symmetry imposition. A subsequent 3D classification with C1 symmetry identified 449,521 particles for final non-uniform refinement and local refinement with recentering. The final reconstruction was achieved at a global resolution of 3.71 Å (FSC = 0.143) with C3 symmetry imposed. Single-particle cryo-EM processing statistics are summarized in supplementary table 3.

Molecular dynamics (MD) simulation. MD **simulations** were performed to evaluate the structural feasibility of N-terminal α-helix insertion into the central cavity of the D13 trimer. The initial model was generated by manually placing the N-terminal α-helix into the base cavity based on cryo-EM density observations. The system was prepared using **CHARMM-GUI** with default parameters[44]. The protein complex was solvated in a TIP3P water box and neutralized with **150 mM NaCl**. The **CHARMM36m** force field was used for all components. Energy minimization and equilibration were performed using standard protocols. A **500-ns production run** was conducted using the **GROMACS** v2024.4[45] with a 2-fs integration time step. Simulation trajectories were saved every **1 ns** for analysis. Distances between the N-terminal α-helix and F-ring residues (F168, F486, and F487) were measured using built-in GROMACS tools and custom scripts.

Protein structure model building. Model building was proceeded by manually fitting the cryo-EM structure of D13 (PDB ID 7VFD, 7VFE) into our cryo-EM map using UCSF Chimera[46], which served as the initial reference model. The model was subsequently inspected and adjusted in Coot[47], with noncrystallographic symmetry (NCS) constraints applied. Coordinate refinements were performed using the real-space refinement routine in the Phenix software suite[48]. The quality of the final model and map-to-model correlations were evaluated using the Cryo-EM validation tool in Phenix[49]. The maps and models were displayed using UCSF Chimera X for the preparation of the figures[50].

Declarations

Data availability. Atomic coordinates of cryo-EM–derived models have been deposited in the Protein Data Bank under the following PDB accession codes: 9USX (His_6-tagged D13 spherical assembly SPA), 9USY (eGFP–D13 spherical assembly SPA), , 9USU (D13 Twister Mode I SPA), 9USV (D13 Twister Mode II SPA), 9USW (D13 Twister Mode III SPA), 9USZ (D13–$A17_{1-8}$–bound trimer SPA), and 9UT0 (D13–$A17_{1-8}$–bound spherical assembly SPA). Corresponding cryo-EM density maps have been deposited in the Electron Microscopy Data Bank (EMDB) under the following accession codes: EMD-64468 (His_6-tagged D13 spherical assembly STA), EMD- 64469 (D13 Twister assembly STA), EMD-64474 (His_6-tagged D13 spherical assembly SPA), EMD-64475 (eGFP–D13 spherical assembly SPA), EMD-64470 (D13 Twister assembly SPA), EMD-64471 (D13 Twister Mode I SPA), EMD-64472 (D13 Twister Mode II SPA), EMD-64473 (D13 Twister Mode III SPA), EMD-64476 (D13–$A17_{1-8}$–bound trimer SPA), and EMD-64477 (D13–$A17_{1-8}$–bound spherical assembly SPA). Raw image data are available from the corresponding author upon reasonable request.

Acknowledgements

This work was supported by the National Research Foundation (NRF) grants funded by the Ministry of Science and ICT under grant number 2022R1A2C1005885 (to J.H.), and by Brain Korea 21 FOUR program “Education and Research Center for Fostering Pharmaceutical Researchers towards Leading Innovative Growth” at School of Pharmacy, Sungkyunkwan University (to Y.J. and S.K.), and by Korea Basic Science Institute (KBSI) grant C539200 (to H.J.). We thank NEXUS consortium for supporting cryo-EM usage. Cryo-EM data collections were carried out in Sungkyunkwan University Cooperative Center for Research Facilities (CCRC), Institute of Basic Science (IBS) and KBSI. We also thank Global Science experimental Data hub Center (GSDC) at Korea Institute of Science and Technology Information (KISTI) for computing resources and technical support.

Author contributions

J.H., Y.J., S.K. conceived and designed experiments. Y.J., S.K. and S-N.L. performed molecular cloning, protein purification and cryo-EM sample preparation. J.H., B.R. and H.J. carried out cryo-EM data collection. Y.J. and S.K. processed cryo-EM data and built structure models. J.H.S. performed molecular cloning of eGFP-D13 construct. E.S.K synthesized and characterized A17 peptide. Y.H.K. and D.G.J. provided advice on peptide synthesis and eGFP-D13 production, respectively. J.H. supervised the project. J.H., Y.J., S.K., S-N. L. and E.S.K. wrote the manuscript. All authors analyzed results and contributed to writing the paper.

Conflict of interests

The authors declare no competing interests.

References

1. Moore, Z. S., Seward, J. F. & Lane, J. M. Smallpox. *Lancet* **367**, 425-435 (2006).

2. Meyer, H., Ehmann, R. & Smith, G. L. Smallpox in the Post-Eradication Era. *Viruses* **12** (2020).
3. Dales, S. & Siminovitch, L. The development of vaccinia virus in Earle's L strain cells as examined by electron microscopy. *J Biophys Biochem Cytol* **10**, 475-503 (1961).
4. Condit, R. C., Moussatche, N. & Traktman, P. In a nutshell: structure and assembly of the vaccinia virion. *Adv Virus Res* **66**, 31-124 (2006).
5. Liu, L., Cooper, T., Howley, P. M. & Hayball, J. D. From crescent to mature virion: vaccinia virus assembly and maturation. *Viruses* **6**, 3787-3808 (2014).
6. Moss, B. Poxvirus membrane biogenesis. *Virology* **479-480**, 619-626 (2015).
7. Weisberg, A. S. *et al.* Enigmatic origin of the poxvirus membrane from the endoplasmic reticulum shown by 3D imaging of vaccinia virus assembly mutants. *Proc Natl Acad Sci U S A* **114**, E11001-E11009 (2017).
8. Bahar, M. W., Graham, S. C., Stuart, D. I. & Grimes, J. M. Insights into the evolution of a complex virus from the crystal structure of vaccinia virus D13. *Structure* **19**, 1011-1020 (2011).
9. Hyun, J. K. *et al.* Membrane remodeling by the double-barrel scaffolding protein of poxvirus. *PLoS Pathog* **7**, e1002239 (2011).
10. Heuser, J. Deep-etch EM reveals that the early poxvirus envelope is a single membrane bilayer stabilized by a geodetic "honeycomb" surface coat. *J Cell Biol* **169**, 269-283 (2005).
11. Chichon, F. J. *et al.* Membrane remodelling during vaccinia virus morphogenesis. *Biol Cell* **101**, 401-414 (2009).
12. Bisht, H., Weisberg, A. S., Szajner, P. & Moss, B. Assembly and disassembly of the capsid-like external scaffold of immature virions during vaccinia virus morphogenesis. *J Virol* **83**, 9140-9150 (2009).
13. Szajner, P., Weisberg, A. S., Lebowitz, J., Heuser, J. & Moss, B. External scaffold of spherical immature poxvirus particles is made of protein trimers, forming a honeycomb lattice. *Journal of Cell Biology* **170**, 971-981 (2005).
14. Chlanda, P., Carbajal, M. A., Cyrklaff, M., Griffiths, G. & Krijnse-Locker, J. Membrane rupture generates single open membrane sheets during vaccinia virus assembly. *Cell Host Microbe* **6**, 81-90 (2009).
15. Sodeik, B. *et al.* Assembly of vaccinia virus: role of the intermediate compartment between the endoplasmic reticulum and the Golgi stacks. *J Cell Biol* **121**, 521-541 (1993).
16. Unger, B., Mercer, J., Boyle, K. A. & Traktman, P. Biogenesis of the vaccinia virus membrane: genetic and ultrastructural analysis of the contributions of the A14 and A17 proteins. *J Virol* **87**, 1083-1097 (2013).
17. Duan, H. *et al.* Identification of core therapeutic targets for Monkeypox virus and repurposing potential of drugs: A WEB prediction approach. *PLoS One* **19**, e0303501 (2024).
18. Vanslyke, J. K., Lee, P., Wilson, E. M. & Hruby, D. E. Isolation and analysis of vaccinia virus previrions. *Virus Genes* **7**, 311-324 (1993).

19. Hernandez-Gonzalez, M., Calcraft, T., Nans, A., Rosenthal, P. B. & Way, M. A succession of two viral lattices drives vaccinia virus assembly. *PLoS Biol* **21**, e3002005 (2023).
20. Hyun, J., Matsunami, H., Kim, T. G. & Wolf, M. Assembly mechanism of the pleomorphic immature poxvirus scaffold. *Nat Commun* **13**, 1704 (2022).
21. Kim, S., Ko, S., Kim, M., Jang, Y. & Hyun, J. Cryo-EM structure of orf virus scaffolding protein orfv075. *Biochem Biophys Res Commun* **728**, 150334 (2024).
22. Garriga, D. *et al.* Structural basis for the inhibition of poxvirus assembly by the antibiotic rifampicin. *P Natl Acad Sci USA* **115**, 8424-8429 (2018).
23. Charity, J. C., Katz, E. & Moss, B. Amino acid substitutions at multiple sites within the vaccinia virus D13 scaffold protein confer resistance to rifampicin. *Virology* **359**, 227-232 (2007).
24. Coulibaly, F. Structure of the poxvirus core. *Nat Struct Mol Biol* **31**, 1001-1003 (2024).
25. Datler, J. *et al.* Multi-modal cryo-EM reveals trimers of protein A10 to form the palisade layer in poxvirus cores. *Nat Struct Mol Biol* (2024).
26. Liu, J. *et al.* The palisade layer of the poxvirus core is composed of flexible A10 trimers. *Nat Struct Mol Biol* **31**, 1105-1113 (2024).
27. Hong, Y. *et al.* Molecular architecture of monkeypox mature virus. *Cell Discov* **10**, 108 (2024).
28. Traktman, P., Caligiuri, A., Jesty, S. A., Liu, K. & Sankar, U. Temperature-sensitive mutants with lesions in the vaccinia virus F10 kinase undergo arrest at the earliest stage of virion morphogenesis. *J Virol* **69**, 6581-6587 (1995).
29. Novy, K. *et al.* Proteotype profiling unmasks a viral signalling network essential for poxvirus assembly and transcriptional competence. *Nat Microbiol* **3**, 588-599 (2018).
30. Betakova, T., Wolffe, E. J. & Moss, B. Regulation of vaccinia virus morphogenesis: phosphorylation of the A14L and A17L membrane proteins and C-terminal truncation of the A17L protein are dependent on the F10L kinase. *J Virol* **73**, 3534-3543 (1999).
31. Erlandson, K. J. *et al.* Poxviruses Encode a Reticulon-Like Protein that Promotes Membrane Curvature. *Cell Rep* **14**, 2084-2091 (2016).
32. Mirzakhanyan, Y., Jankevics, A., Scheltema, R. A. & Gershon, P. D. Combination of deep XLMS with deep learning reveals an ordered rearrangement and assembly of a major protein component of the vaccinia virion. *mBio* **14**, e0113523 (2023).
33. Tonnemacher, S. *et al.* Vaccinia virus H7-protein is required for the organization of the viral scaffold protein into hexamers. *Sci Rep* **12**, 13007 (2022).
34. Rizk, J. G., Lippi, G., Henry, B. M., Forthal, D. N. & Rizk, Y. Prevention and Treatment of Monkeypox. *Drugs* **82**, 957-963 (2022).
35. Vernuccio, R. *et al.* Structural insights into tecovirimat antiviral activity and poxvirus resistance. *Nat Microbiol* **10**, 734-748 (2025).
36. Burt, A. *et al.* An image processing pipeline for electron cryo-tomography in RELION-5. *FEBS Open Bio* **14**, 1788-1804 (2024).

37. Zheng, S. Q. *et al.* MotionCor2: anisotropic correction of beam-induced motion for improved cryo-electron microscopy. *Nat Methods* **14**, 331-332 (2017).
38. Rohou, A. & Grigorieff, N. CTFFIND4: Fast and accurate defocus estimation from electron micrographs. *J Struct Biol* **192**, 216-221 (2015).
39. Mastronarde, D. N. & Held, S. R. Automated tilt series alignment and tomographic reconstruction in IMOD. *J Struct Biol* **197**, 102-113 (2017).
40. Buchholz, T. O. *et al.* Content-aware image restoration for electron microscopy. *Methods Cell Biol* **152**, 277-289 (2019).
41. Ermel, U. H., Arghittu, S. M. & Frangakis, A. S. ArtiaX: An electron tomography toolbox for the interactive handling of sub-tomograms in UCSF ChimeraX. *Protein Sci* **31**, e4472 (2022).
42. Chen, M. *et al.* A complete data processing workflow for cryo-ET and subtomogram averaging. *Nat Methods* **16**, 1161-1168 (2019).
43. Punjani, A., Rubinstein, J. L., Fleet, D. J. & Brubaker, M. A. cryoSPARC: algorithms for rapid unsupervised cryo-EM structure determination. *Nat Methods* **14**, 290-296 (2017).
44. Jo, S., Kim, T., Iyer, V. G. & Im, W. CHARMM-GUI: a web-based graphical user interface for CHARMM. *J Comput Chem* **29**, 1859-1865 (2008).
45. Abraham, M. J. *et al.* GROMACS: High performance molecular simulations through multi-level parallelism from laptops to supercomputers. *SoftwareX* **1-2**, 19-25 (2015).
46. Pettersen, E. F. *et al.* UCSF chimera - A visualization system for exploratory research and analysis. *Journal of Computational Chemistry* **25**, 1605-1612 (2004).
47. Emsley, P., Lohkamp, B., Scott, W. G. & Cowtan, K. Features and development of Coot. *Acta Crystallogr D Biol Crystallogr* **66**, 486-501 (2010).
48. Liebschner, D. *et al.* Macromolecular structure determination using X-rays, neutrons and electrons: recent developments in Phenix. *Acta Crystallogr D Struct Biol* **75**, 861-877 (2019).
49. Afonine, P. V. *et al.* New tools for the analysis and validation of cryo-EM maps and atomic models. *Acta Crystallogr D Struct Biol* **74**, 814-840 (2018).
50. Meng, E. C. *et al.* UCSF ChimeraX: Tools for structure building and analysis. *Protein Sci* **32** (2023).

Figures

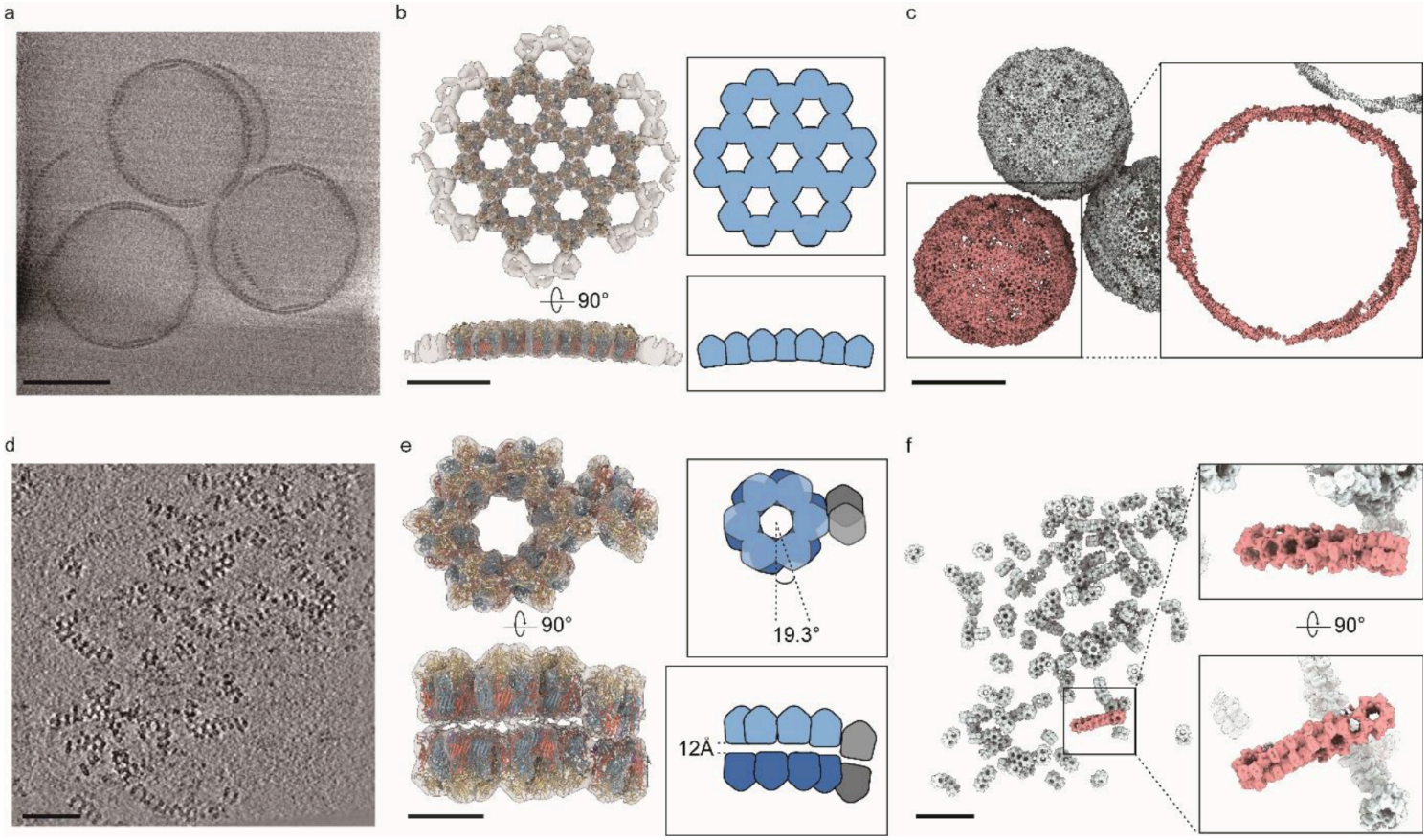


Figure 1

Tomographic reconstructions and subtomogram averages of *in vitro* assembly products of D13. a, A representative tomographic slice of vaccinia virus (VACV) scaffold-like particle (SLP). **b,** Subtomogram averaging (STA) map of lattice patches in the SLP, showing a hexagonal arrangement of D13 trimers. Atomic models of individual D13 trimers (PDB: 7VFD) are fitted into the map. The panels on the right show schematic illustrations of honeycomb-shaped lattice patch with planar curvature that tapers towards the base of the trimers. **c**, The STA map plotted back into the tomogram of the SLP, showing overall dimensions and morphology reminiscent of the scaffold layer observed in authentic vaccinia virus (VACV) immature virions (IVs). Zoomed-in boxed regions display a clipping view of a particle, showing multilayered scaffold lattices in the absence of an underlying viral membrane of theauthentic IVs. **d,** A tomographic slice showing short rod-like assemblies arranged in linear arrays of hexagonal patches, resembling structures observed in the intracytoplasmic inclusion bodies (IBs) of VACV-infected cells. **e,** STA map of repeating units in the twister with fitted atomic models, showing two vertically apposed hexagonal rings, each composed of six D13 trimers. Additional trimers are tethered at the ring periphery and are clearly displaced out of the horizontal plane. The panels on the right showschematic diagramsillustrating the two vertically stacked hexagonal rings, colored sky blue (upper) and blue (lower). One ring is rotated by 19.3° relative to the other, with a vertical gap of ~12 Å. **f**, The STA map plotted back into the tomogram showing a twisted, chain-like ultrastructure composed of stacked hexagonal ring pairs. Zoomed-in boxed regions highlight the rotational offset between rings, supporting their identification as the “twisters.” Fitted D13 trimers are shown in ribbon representation, highlighting

the N- and C-terminal jelly roll domains (blue and red), head domain (yellow), and N-terminal α-helix (purple). Scale bars, 200 nm in **a** and **c**, 20 nm in **b**, 100 nm in **d** and **f**, and 10 nm in **e**.

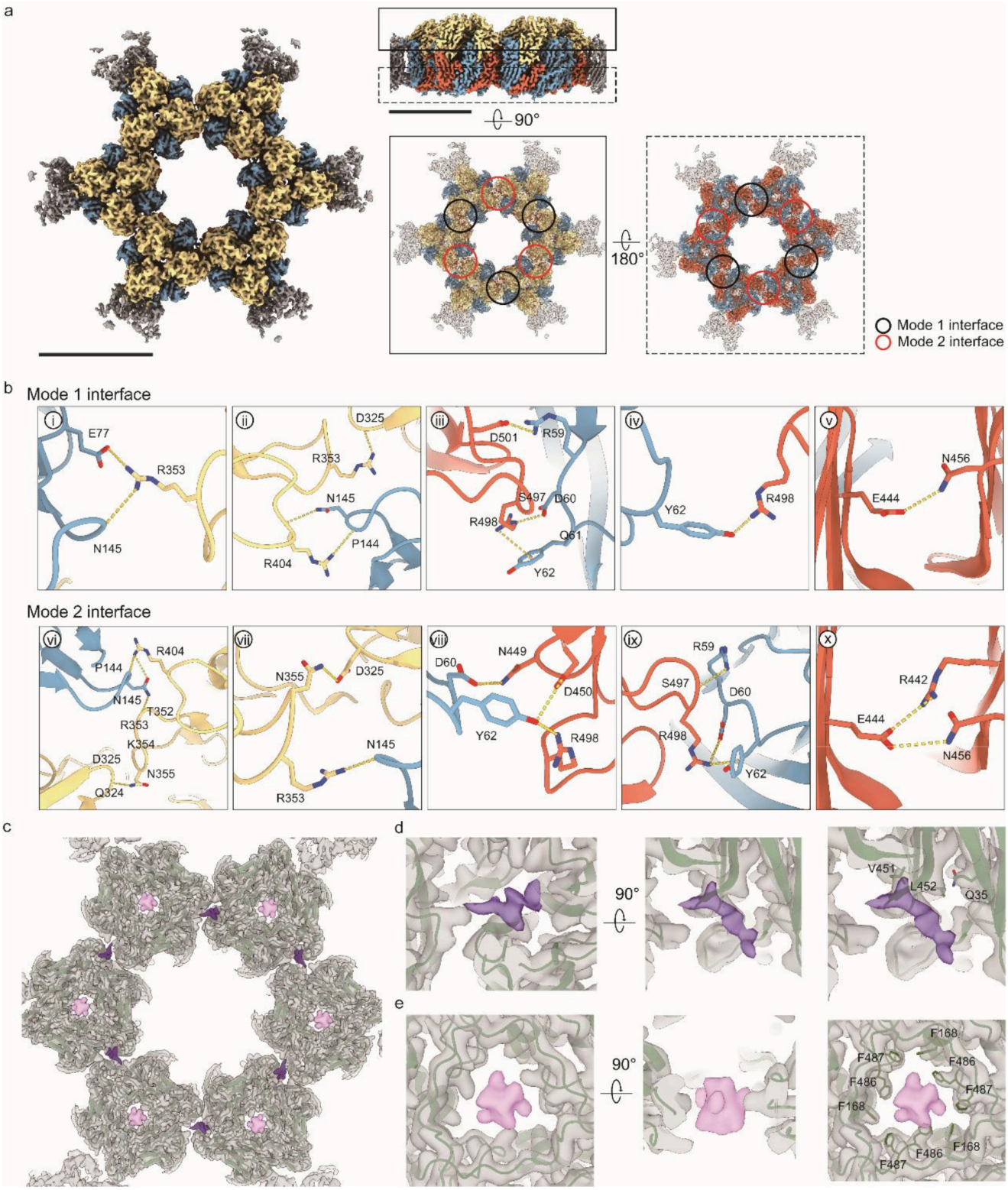


Figure 2

Single-particle cryo-EM structure of SLP lattice. a, 3D reconstruction of the hexagonal lattice patch of SLP. Insets show slabs along the vertical axis of the map. Head-to-head and base-to-base interfaces are

marked with black (mode 1) and red (mode 2) circles. **b**, Intertrimer interactions at mode 1 (top row) and mode 2 (bottom row) interfaces that are primarily electrostatic. Structures are shown in ribbon representation. Key residues involved in intertrimeric contacts are shown in stick representation. **c**, Additional map densities not attributable to the previously reported D13 structure. One is located between two adjacent trimers (purple). The other is found in the central cavity at the trimer base (pink), corresponding to the rifampicin-binding site. **d**, Close-up view of the density between the bases of interacting trimers, presumably representing the N-terminal α-helix of D13. **e**, Close-up view of the base cavity density (pink), located near hydrophobic residues known to be critical for rifampicin binding. Scale bar, 10nm.

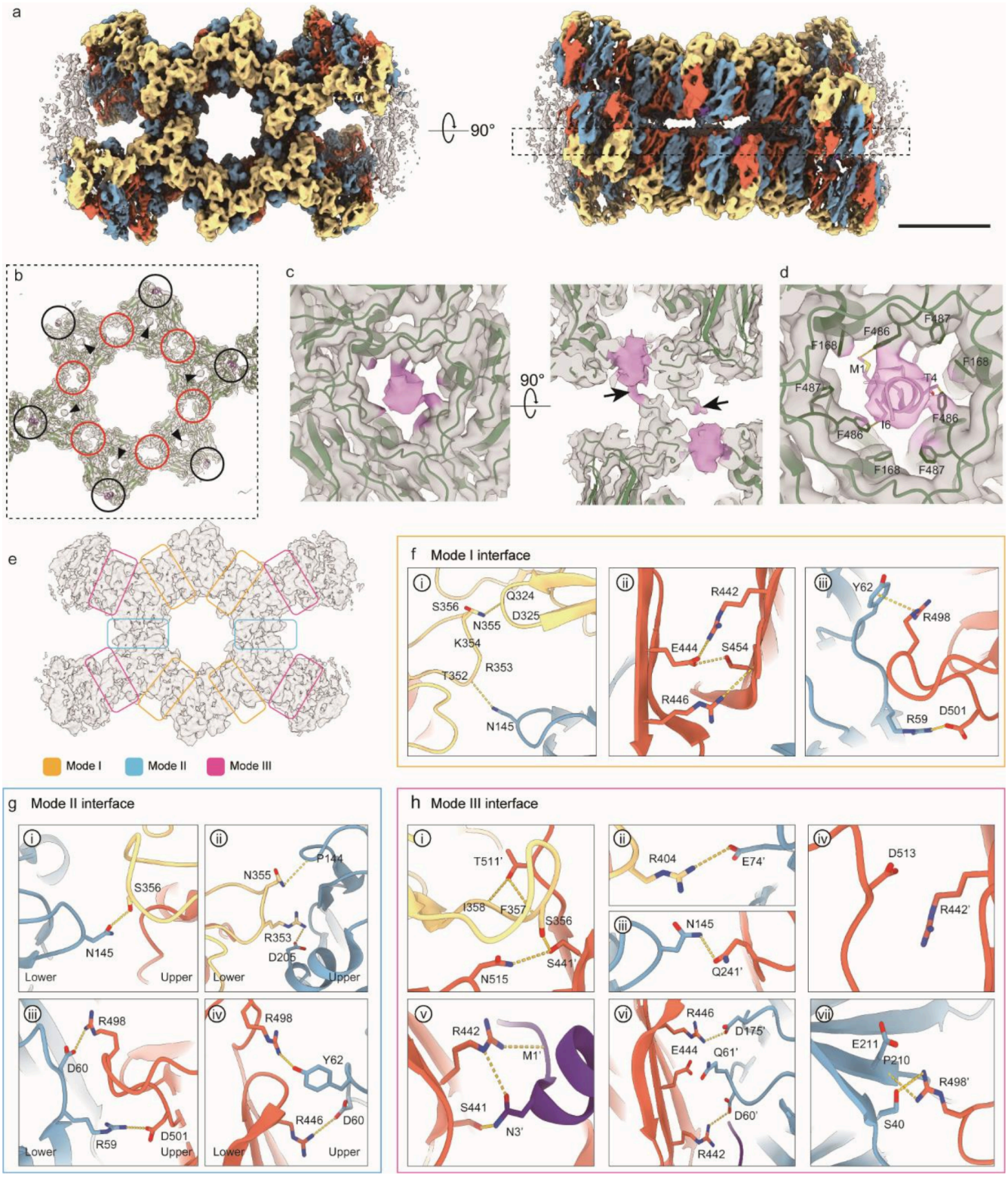


Figure 3

Single-particle cryo-EM structure of the twister assembly. a, 3D reconstruction of repeating units of the twister exhibiting two apposed hexagonal rings of D13 trimers with twisted extensions by additional trimers on both sides of the ring. **b**, Cross section along the vertical interface (marked by dashed box) showing the absence of the N-terminal helix between laterally interacting trimers within the hexagonal ring (red circles), the presence of intact helices at the periphery (black circles) and additional map

density at the base cavities (arrowheads). **c**, Enlarged view of the additional map density (pink) at the base cavity of a D13 trimer (green). At higher contour level ($\sigma > 2.0$), density connection between the N-terminus of a trimer and the base cavity of vertically opposing D13 trimer is visible (arrow). **d**, Manually fitted N-terminal helix structure into the additional density, suggesting potential hydrophobic interactions with phenylalanine residues within the base cavity. **e**, Three intertrimeric interface modes marked by yellow, cyan and magenta boxes. **f–h**, Intertrimeric interactions at mode I, II and III interfaces, respectively. Structures and key residues are shown in ribbon and stick representations. Scale bar, 10 nm.

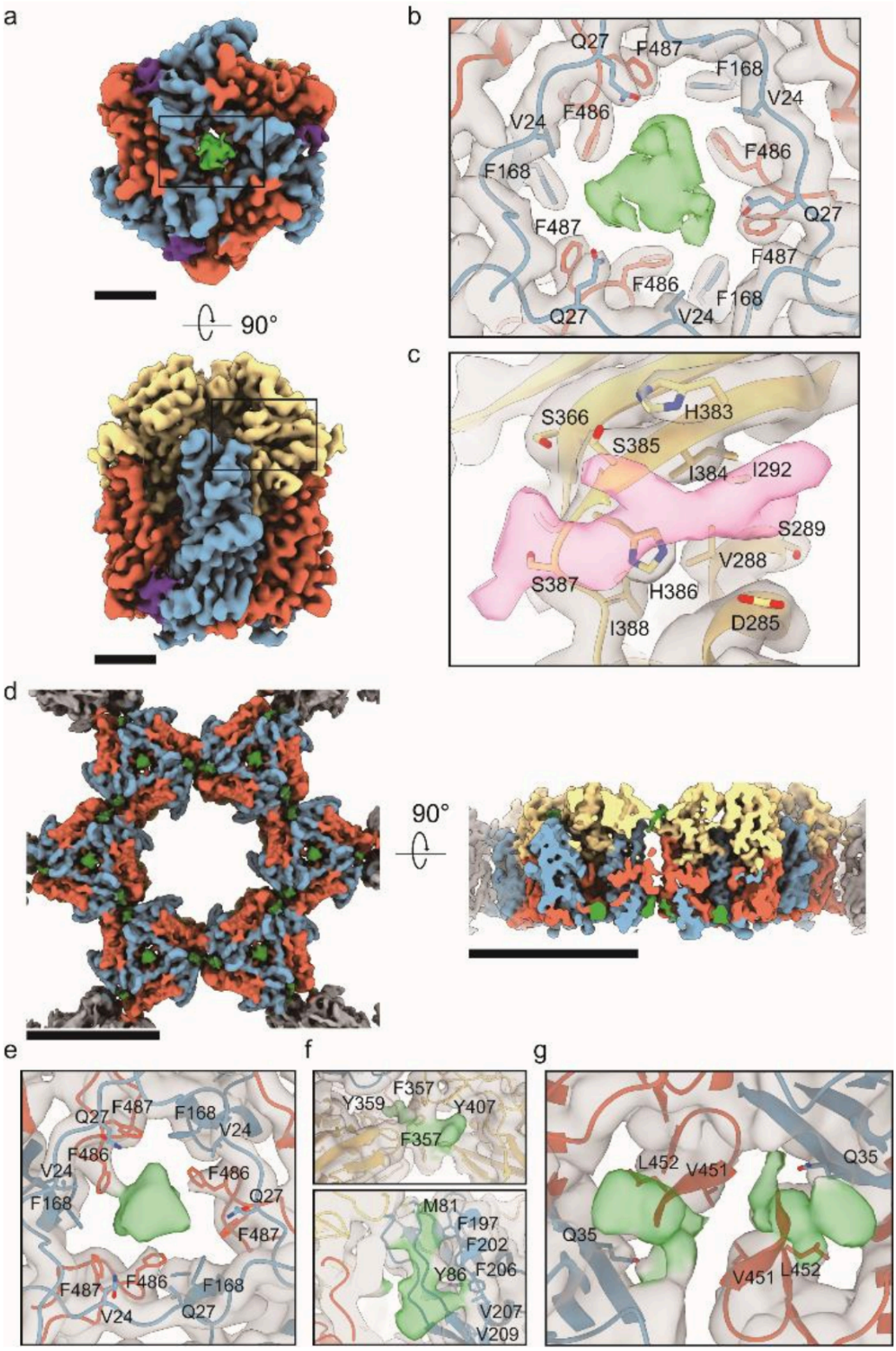


Figure 4

Cryo-EM structures of D13-A17$_{1-8}$ complex in its singular form and SLP. a, 3D reconstruction of the A17$_{1-8}$-bound D13 trimer. An extra density is observed in the base cavity (green). Boxed regions indicate the base cavity and head domain groove, which are enlarged in b and c, respectively. **b**, Close-up view of the base cavity showing the A17$_{1-8}$ density (green) surrounded by residues V24, Q27, F168, F486, and F487. **c**, Close-up view of the head domain, where an additional density (pink) is observed within a

hydrophobic groove. **d**, 3D reconstruction of the $A17_{1-8}$-bound SLP showing a hexagonal lattice arrangement. Extra densities (shown in green) are observed in the head domain, base cavities and N-terminal α-helix binding pockets. **e**, The extra density observed in the central cavity of the SLP base (green), consistent with that seen in the singular trimer. **f**, A close-up view of the head-to-head intertrimeric interface, where additional densities are observed, surrounded by hydrophobic residues. **g**, Close-up view of the N-terminal α-helix pocket, where an additional density (green) is observed adjacent to hydrophobic side chains. Scale bars, 2 nm in **a**, 10 nm in **d**.

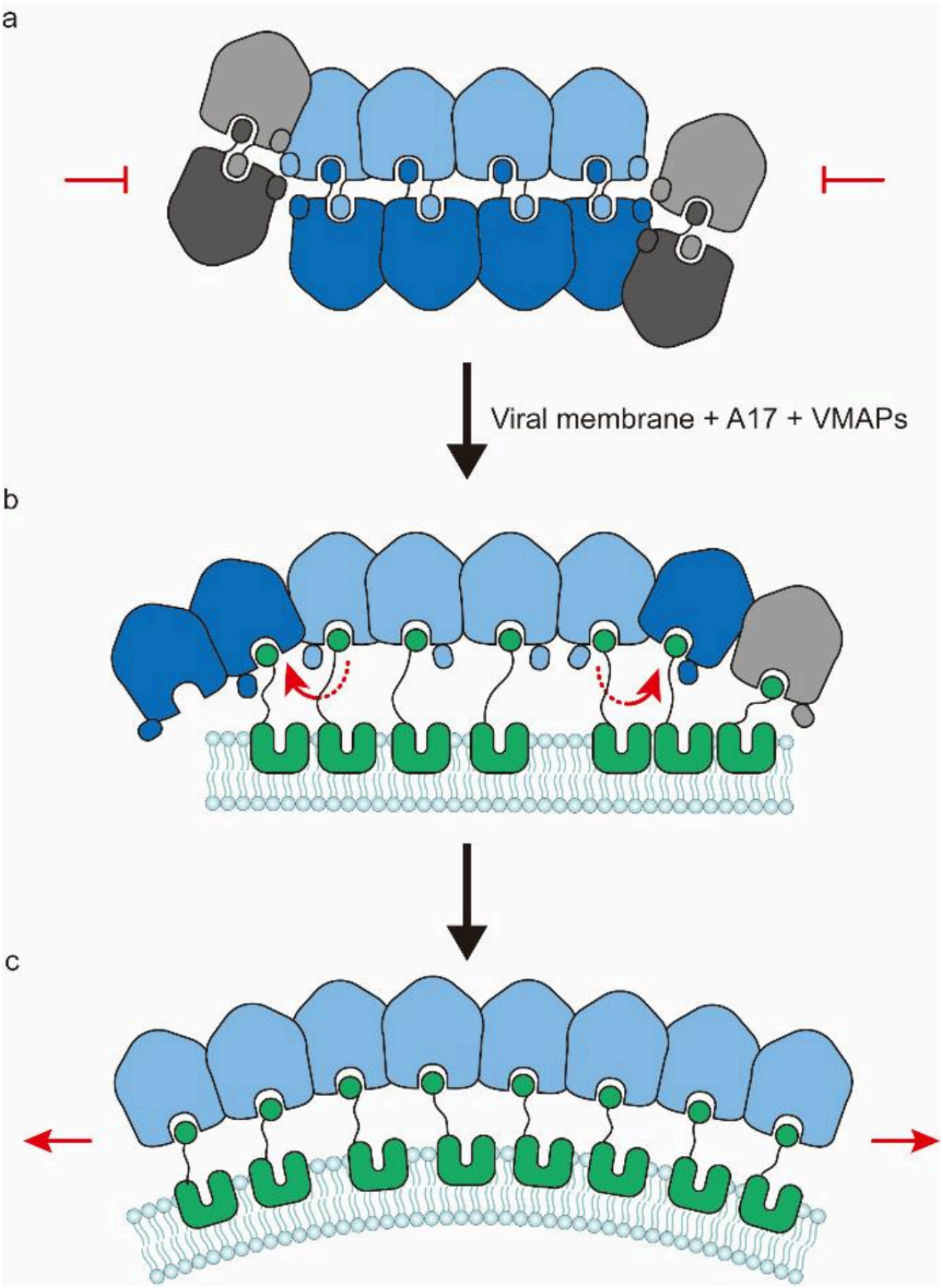


Figure 5

Proposed mechanism of transition from the D13 pre-assembly complex to scaffold lattice of VACV IV. **a**, Within the virus factory of VACV-infected cell cytoplasm, D13 exists as aggregated twister complex composed of two apposed rings of a sextet of trimers (colored light blue and dark blue for upper and lower ring, respectively). Domain swapping of N-terminal α-helix between vertically opposing trimers and twisted tethering of additional trimers (shown in grey) stabilize the complex. This architecture prevents continuous expansion of scaffold lattice (shown by red blocked arrow), hence preventing the production of empty shells in the absence of viral membrane. **b**, Viral membrane, stabilized by VMAPs and containing A17 (shown in green), disengages vertically interacting D13 trimers (shown by red arrow) via replacing the N-terminal α-helix from base cavity with N-terminal tail of A17. Monolayered lattice patches interact laterally and subsequently displace residual N-terminal helices that were previously intact at the periphery of twister complex. **c**, D13 trimers continue to assemble laterally on the viral membrane (shown by red arrow), generating a mild curvature that results from intertrimeric torsion. In turn, the linkage between D13 and A17 allows for the viral membrane remodeling into spherical morphology.

Supplementary Files

This is a list of supplementary files associated with this preprint. Click to download.

- Jangetalsupplmentaryinformation.docx
- Extendeddata.docx